Supplementary Information of

Boosting silica micro-rod *Q* factor to 8.28×10^9 for fully stabilizing a soliton microcomb

Teng Tan[1,2,3,#], Ting-Yang Pan[1,#], Bing Duan[1,#], Bing Chang[2], Fan Tang[2], Yong-Jun Huang[2], Ying-Zhan Yan[4], Da-Quan Yang[1,*], Shan-Guo Huang[1,*], and Bai-Cheng Yao[2,*]

[1]*State Key Laboratory of Information Photonics and Optical Communications, Beijing University of Posts and Telecommunications, Beijing 100876, China.*

[2]*Key Laboratory of Optical Fiber Sensing and Communications* (*Education Ministry of China*), *University of Electronic Science and Technology of China, Chengdu 611731, China.*

[3]*Institute of Electronic and Information Engineering of UESTC, Guangdong 523808, China.*

[4]*Information Science Research Institute, China Electronics Technology Group Corporation, Beijing 100876, China.*

[#]**These authors contributed equally:** Teng Tan, Ting-Yang Pan, Bing Duan

***Corresponding authors:** ydq@bupt.edu.cn; shghuang@bupt.edu.cn; yaobaicheng@uestc.edu.cn

Supplementary Note S1: Theoretical analysis and simulations.

S1.1 The calculation of quality factor of microcavity.

The quality factor (Q) is an important parameter to characterize the performance of microcavities, which is defined by the classical formula[1]:

$$Q = \omega_0/\kappa = \omega_0\tau \tag{S1}$$

where ω_0 is the angular frequency of the resonance, κ is overall loss rate of the system which consists of both the intrinsic loss rate κ_0 and the coupling loss rate κ_{ex} and τ is the total photon lifetime.

The loaded Q factor (Q_L) can be expressed as:

$$Q_L^{-1} = Q_0^{-1} + Q_{ex}^{-1} \tag{S2}$$

where Q_0 is the intrinsic loss of microcavity, mainly including the radiative loss ($1/Q_{rad}$), the scattering loss ($1/Q_{sca}$), the materials absorption loss ($1/Q_{abs}$) and the contaminant

loss ($1/Q_{cont}$). Q_{ex} is the external Q factor which characterizes the coupling loss of microcavity. Therefore, Q_L takes into account the total loss, including coupling loss and the intrinsic loss of the microcavity.

According to **Eq.(S1)**, the Q-factor of a microcavity can be obtained by measuring the overall loss rate κ or the total photon lifetime τ. Typically, the above two parameters can be extracted from the transmission spectrum of the cavity resonance measured by scanning a CW laser over it. For microcavities with the Q-factor less than 10^8, corresponding a resonance linewidth in the megahertz level, slow scanning of CW laser frequency is used for measuring the transmission spectrum and κ can be obtained by Lorentz fitting the resonance. While, for microcavities with ultra-high Q-factor, the resonance linewidth is already comparable with that of the probe laser. In this case, the instability of the probe laser during slow scanning will affect the test accuracy of resonance linewidth, resulting in inaccurate Q-factor. Therefore, the probe laser frequency tuning within the linewidth could be faster than the intracavity photon lifetime, which leaves a ringdown profile at the ending edge of the resonance.

The time evolution of the intracavity field of one resonant mode could be described as a simple harmonic oscillator model[2]:

$$\frac{\partial A}{\partial t} = i\omega_0 A - \frac{\kappa}{2} A + \sqrt{\kappa_{ex}} s_{in} \tag{S3}$$

where $A = a\exp[i\varphi(t)]$ is the time evolution of the intracavity field and $s_{in} = s_0\exp[i\varphi(t)]$ is the external source injection.

When the laser frequency tuning with respect to its initial value ω_i is slowly changed compared with the intracavity photon lifetime, we have $\varphi(t) = \omega_i t$ and the variation of **Eq. (S3)** could be:

$$\frac{\partial a}{\partial t} = i\delta\omega a - \frac{\kappa}{2} a + \sqrt{\kappa_{ex}} s_0 \tag{S4}$$

where $\delta\omega = \omega_0 - \omega_i$ is the laser detuning. By setting $\partial a/\partial t = 0$, the solution of **Eq. (S4)** can be obtained as follows:

$$a = \frac{\sqrt{\kappa_{ex}} s_0}{-\left(i\delta\omega - \kappa/2\right)} \tag{S5}$$

In contrast, in the condition that the laser frequency tuning is comparable with the photon lifetime, we have $\varphi(t) = (\omega_i + V_s t/2)t$ and the variation of **Eq. (S3)** could be:

$$\frac{\partial a}{\partial t} = i\left(\delta\omega - V_s t\right)a - \frac{\kappa}{2}a + \sqrt{\kappa_{ex}}s_0 \tag{S6}$$

where V_s is the tuning speed of the laser frequency. The solution of **Eq. (S6)** can be obtained by integration.

$$a = \sqrt{\kappa_{ex}}s_0 \exp\left(i\omega_0 t - \frac{\kappa}{2}t\right)\left[f(t) - f(0) - \frac{1}{i\delta\omega - \frac{\kappa}{2}}\right] \tag{S7}$$

with

$$f(t) = -\sqrt{\frac{i\pi}{2V_s}}\exp\left[i\frac{\left(i\delta\omega - \kappa/2\right)^2}{2V_s}\right]\mathrm{erf}\left[-i\frac{i\left(\delta\omega - V_s t\right) - \kappa/2}{\sqrt{2iV_s}}\right] \tag{S8}$$

where erf(z) is the complex error function.

The transmission spectrum T can be calculated as follows:

$$T = \left|\frac{-s_0 + \sqrt{\kappa_{ex}}a}{s_0}\right|^2 \tag{S9}$$

For slow scanning case, the transmission spectrum of the microcavity shows a standard Lorentz profile as a function of the laser detuning $\delta\omega$. **Fig. S1a** shows the transmission spectrum with an intrinsic Q of 1×10^7 and a load Q of 5×10^6. For fast scanning case, the transmission spectrum of the microcavity shows a standard ringdown profile as a function of the laser scanning time t. **Fig. S1b** shows the transmission spectrum with an intrinsic Q of 1×10^{10}, a load Q of 5×10^8 and a tuning speed of 100 GHz/s.

Fitting the experimental data with **Eq. (S9)** would deterministically return the coupling rate κ_{ex} as part of the overall loss rate κ, such that the coupling regime of the cavity (over-, critical-, or under-coupling) can be clearly distinguished.

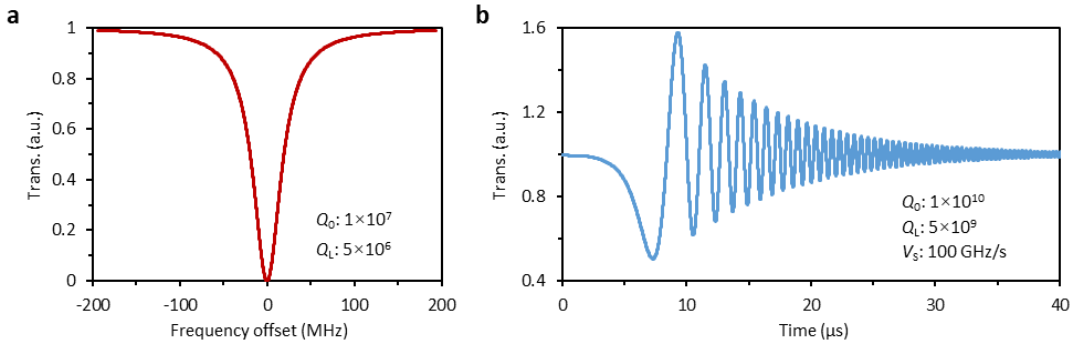

Fig. S1. The simulations of transmission spectrum of microcavity. a, For low-Q microcavities and slow scanning of the probe laser, the transmission spectrum exhibits

a Lorentz profile. **b,** For high-Q microcavities and fast scanning of the probe laser, the transmission spectrum exhibits a ringdown profile.

S1.2 The calculation of material absorption loss of microcavity.

S1.2.1 Absorption loss of microcavity based on materials.

Through the cavity-enhanced photothermal spectroscopy[3], the material-limited Q factor (Q_{abs}) can be derived by the following equation:

$$Q_{abs} = \frac{2\eta}{\kappa}\omega_0\left(\frac{\delta f}{\delta T}C_0\right)\Big/\frac{d\Delta f}{dP_{in}} \tag{S10}$$

where $\eta = Q_{\mathrm{L}}/Q_{\mathrm{e}}$ is the coupling ratio, $\kappa = \kappa_0 + \kappa_{\mathrm{ex}}$ is the total decay rate where κ_0 and κ_{ex} denote the intrinsic resonator decay rate and the coupling rate, ω_0 is the resonant frequency, C_0 is the heat capacity of the microcavity, $\delta f/\delta T$ is the resonant tuning coefficient, Δf is the full width at half maximum (FWHM) of resonance and P_{in} is the launched-in optical power. The relationship between material absorption loss α_{abs} (dB/km) and material-limited Q_{abs} is expressed as[3]:

$$\alpha_{abs} = \frac{4343}{Q_{abs}}\frac{2\pi n}{\lambda_0} \tag{S11}$$

where n is the refractive index of material and λ_0 is the resonant wavelength. Therefore, the absorption loss α_{abs} (dB/km) can be given by:

$$\alpha_{abs} = 4343\frac{1}{Q_L\eta}\frac{\pi n}{C_0\lambda_0}\left(\frac{\delta f}{\delta T}\right)^{-1}\frac{d\Delta f}{dP_{in}} \tag{S12}$$

S1.2.2 The Simulation of heat capacity C_0 of different order modes.

In this experiment, it is a challenge to determine the exact field distribution of the employed resonant mode. In the simulation, we assume the fundamental mode represents the resonant mode used in the experiment. However, this assumption introduces some errors since different modes exhibit different field distributions. Here, the potential errors introduced by this assumption are analyzed. The field distributions of ten modes are calculated, encompassing five different TE and TM modes, as shown in **Fig. S2a.** Subsequently, by adding the heat source, the thermal steady-state is investigated of these ten modes, and the corresponding heat capacity C_0 of different modes is summarized in **Fig. S2b**. Through the comparison of the heat capacity of ten different modes within the same geometric structure, it is observed that the heat capacity associated with the fundamental mode is greater than that of other higher-order modes.

In addition, among the same order modes, TE modes exhibit higher heat capacity compared to TM modes. According to **Eq. (S2 & S3)**, it can be inferred that larger heat capacity corresponds to smaller material absorption loss under identical conditions. This implies that selecting TE modes within the fundamental mode (C_0 = 90.43 K/W) enables a smaller material absorption loss.

S1.3 The calculation of radiation loss of microcavity.

$1/Q_{rad}$ denotes intrinsic radiative (curvature) losses and the radiation-limited Q factor (Q_{rad}) can be approximated as[4]:

$$Q_{rad} = \frac{1}{2}\left(l+\frac{1}{2}\right) n^{(1-2b)} \left(n^2-1\right)^{1/2} e^{2T_l} \tag{S13}$$

$$T_l = \left(l+\frac{1}{2}\right)\left(\eta_l - \tanh\eta_l\right) \tag{S14}$$

$$\eta_l = \arccos h\left\{ n\left[1-\left(t_q^0 \xi + \frac{l^{1-2b}}{\sqrt{l^2-1}\left(l+\frac{1}{2}\right)} \right)\right]^{-1} \right\} \tag{S15}$$

$$\xi = \left[\frac{l+1/2}{2}\right]^{1/2} \tag{S16}$$

where b=0 (TE) or 1 (TM), $t_q^0$is the q-th zero of the Airy function, q is the radial mode order, q = 1, and $l = 2\pi nr/\lambda$ (r is the curvature radius of the microcavity, λ is the wavelength). Here, we calculated the radiation at various radii (R) of the silica microcavity within the 1550 nm wavelength band. As illustrated in **Fig. S2c**, when the radius is small (R < 10 μm), the radiation loss limits the Q_0 to the 10^{10} level. At this time, radiation loss is the primary factor that reduces Q_0. Since Q_{rad} increases exponentially with radius, the Q_0 factor of the microcavity is no longer constrained by the radiation loss when the radius is larger than 50 μm. In our experiments, the diameter of the silica microcavity reached 3.0 mm, making the radiation loss negligible.

S1.4 The simulation of contaminant loss of microcavity.

Since the microcavity diameter (3 mm) and the possible thickness of the water layer (0.2 nm) differ greatly in size, it is difficult to simulate the relationship between them directly. Therefore, as shown in **Fig. S2d**, we established the microcavity model with various diameters from 0.1 mm to 3.0 mm. As shown in **Fig. S2c**, in the small-diameter microcavity model, it is noted that the diameter of the microcavity still needs

to be greater than 0.04 mm. This is necessary to prevent the Q_0 factor of the microcavity from being affected by radiation loss. The water layer with a thickness of 0.2 nm is used for simulation, and curve fitting is performed.

As illustrated in **Fig.S2e**, the simulation and curve fitting of the large-diameter microcavity are then conducted, showing an overall trend similar to that of the small-diameter microcavity. For the microcavity with a diameter of 3 mm used in this paper and the water layer with a thickness of 1 nm, the Q_0 factor of the microcavity will decrease from 10^{10} to 10^9.

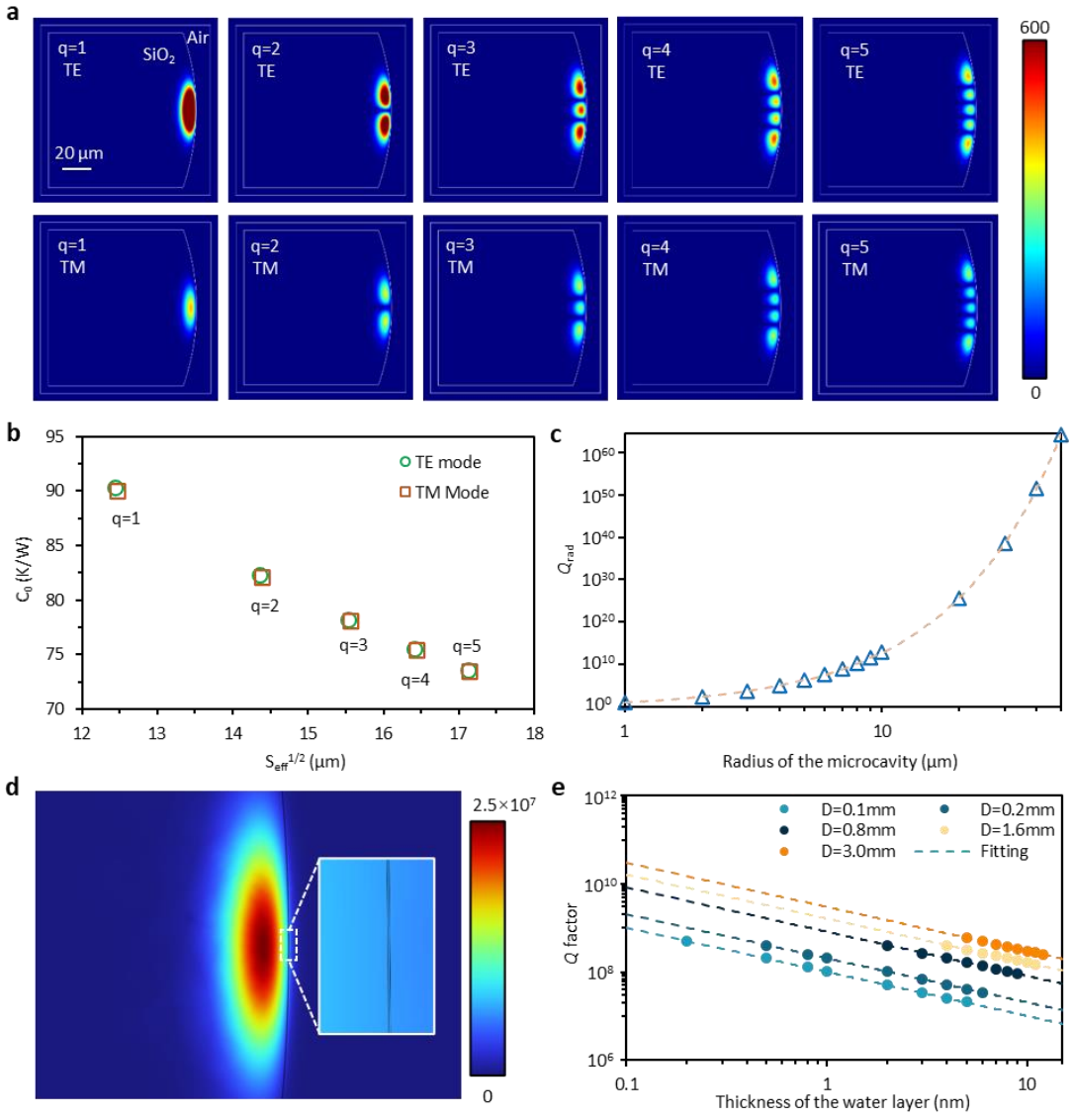

Fig. S2. Numerical calculation and simulation of various losses. a, Mode field distribution diagram of different mode fields. **b**, Plot of heat capacity (C_0) versus the square root of the effective mode area ($S_{eff}^{1/2}$), where q is the axis order number of modes. **c,** Effect of microcavity radius on radiation loss limited Q factor (Q_{rad}). **d**, Mode field distribution diagram of diameter of 0.1mm microcavity with 1 nm water layer. **e**,

Plot of Q factor (Q_0) versus thickness of the water layer of different diameters of microcavities.

Supplementary Note S2: The detailed fabrication and packaging process of the microrod cavities.

S2.1 Fabrication process of the microrod cavities.

Figure S3a shows the schematic of the fabrication platform, and the laser fabrication system is shown in **Fig. S3b**. A low-OH content (< 1 ppm in weight) fused-silica fibre preforms rod with a diameter of 3 mm is used for microcavity fabrication, as displayed in **Fig. S3c**. The fibre preform is mounted on a motor-driven ball-bearing spindle (**Fig. S3b**). The CO_2 laser beams are focused onto the fused silica rod with a ZnSe lens, which is mounted on a computer-controlled translation stage with sub-micrometer resolution. In order to monitor the fabrication process, a microscope with a CCD camera is mounted on top of the silica rod.

The detailed fabrication process is as follows. Firstly, a fibre preforms rod with a length of about 4.5 cm is fixed on the rotating shaft, and the surface is cleaned using ethyl alcohol, (**Fig. S3d**). Then, the left part of the cavity is fabricated by curving the rotating rod with a CO_2 laser powered 18.75 W for 7 seconds (**Fig. S3e**). Subsequently, the same step executes repeat to get the right side of the cavity, while the curving time is decreased to 6 seconds due to the increase in temperature of the whole rod (**Fig. S3f**). Finally, the remaining silica between the two sides confines the optical whispering-gallery mode. To make the surface of the rod much smoother, we decreased the power of the CO_2 laser to 7.5 W to let the laser reflow from one side to the other side three times (**Fig. S3g**). To get the best results, the laser power in the fabrication process should be adjusted to accommodate the size of the preform and the distance between the curving parts. Moreover, with the help of the automated program, the whole fabrication process can be completed in less than one minute by executing the preset parameters.

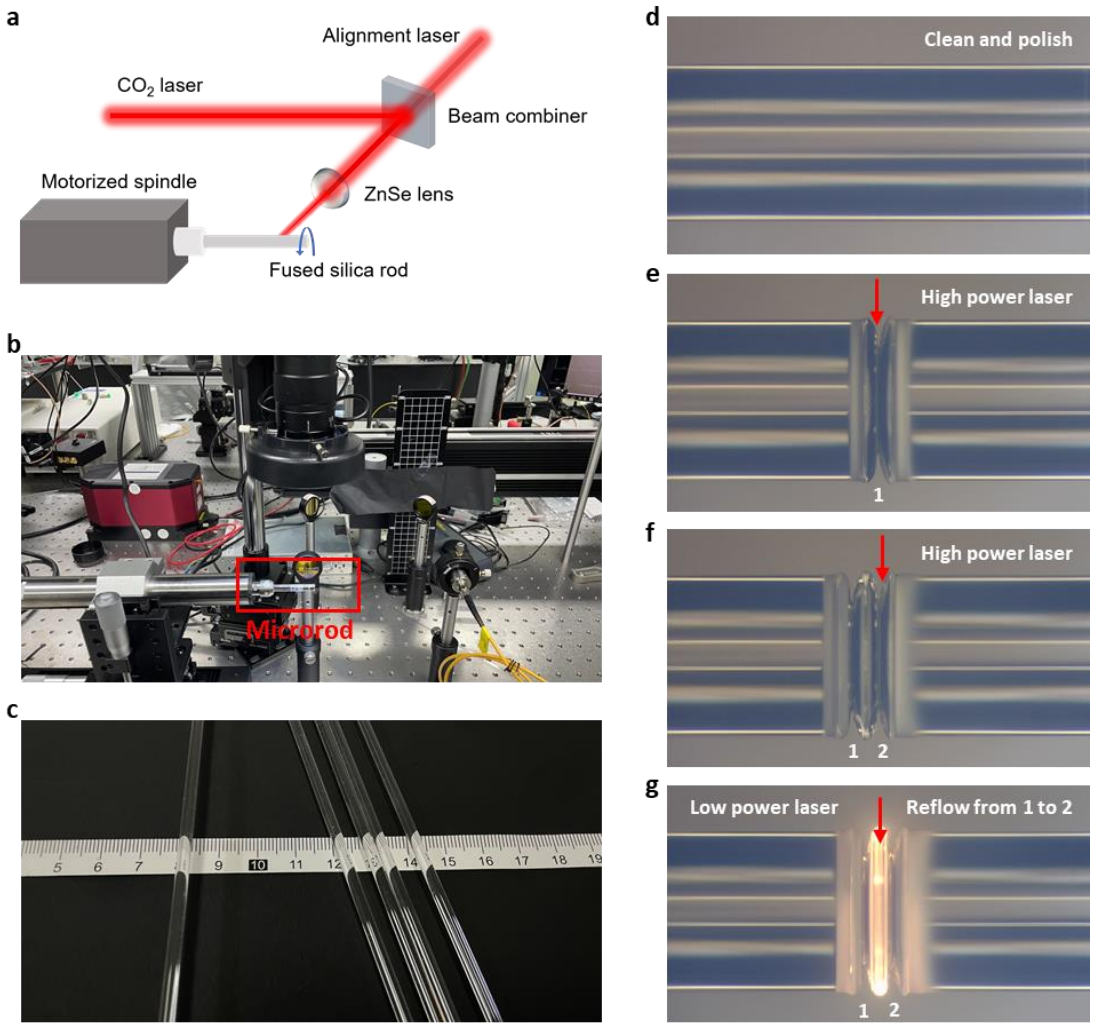

Fig. S3. Fabrication of microrod cavity. a, Schematic drawing of fabrication platform. **b,** Camera picture of the laser fabrication system. **c,** 3mm-diameter silica fibre preforms. **d-g,** Microscope images of the device of sequential fabrications.

S3.2 Packaging process of the microrod cavities.

Figure S4a shows the packaging process of the microrod cavities. The package box is composed of an outer box, an inner box and an aluminum box cover. For stability, the inner box is fixed inside the outer box using screws. The microrod cavity is placed in the groove of the inner box, and the position of the tapered fiber is fine-tuned by a precision three-dimensional nano-positioning platform to ensure the optimal coupling position. Low-loss ultraviolet (UV) adhesive was used to fix the microrod cavity and the coupled tapered optical fiber, and screws were used to fix the lid of the box. Other voids of the packaging box were also sealed with adhesive and glue.

For nitrogen encapsulation, on the side of the outer box of the package box, a

stomatal aperture with a diameter of 3 mm is reserved, and one end of the ventilation tube is passed through the stomatal aperture, and the vent of the ventilation tube is ensured to be inside the package box. The UV adhesive is used to fix the ventilation tube, and the other end of the aluminum ventilation tube is connected with the gas hose through the gas adapter to input nitrogen (concentration >99%), where nitrogen is stored in the cylinder. The pressure reducing valve at the cylinder outlet is connected with the gas hose and controls the nitrogen flow rate.

For temperature heating, the packaged microcavity was placed on a constant temperature heating platform (HANBANG HP-1010) and fixed with thermal conductive silica gel (PINSAI GK-920) to increase heat transfer.

Finally, the microrod cavity is securely housed in a custom aluminum package case, as shown in **Fig.S4f**.

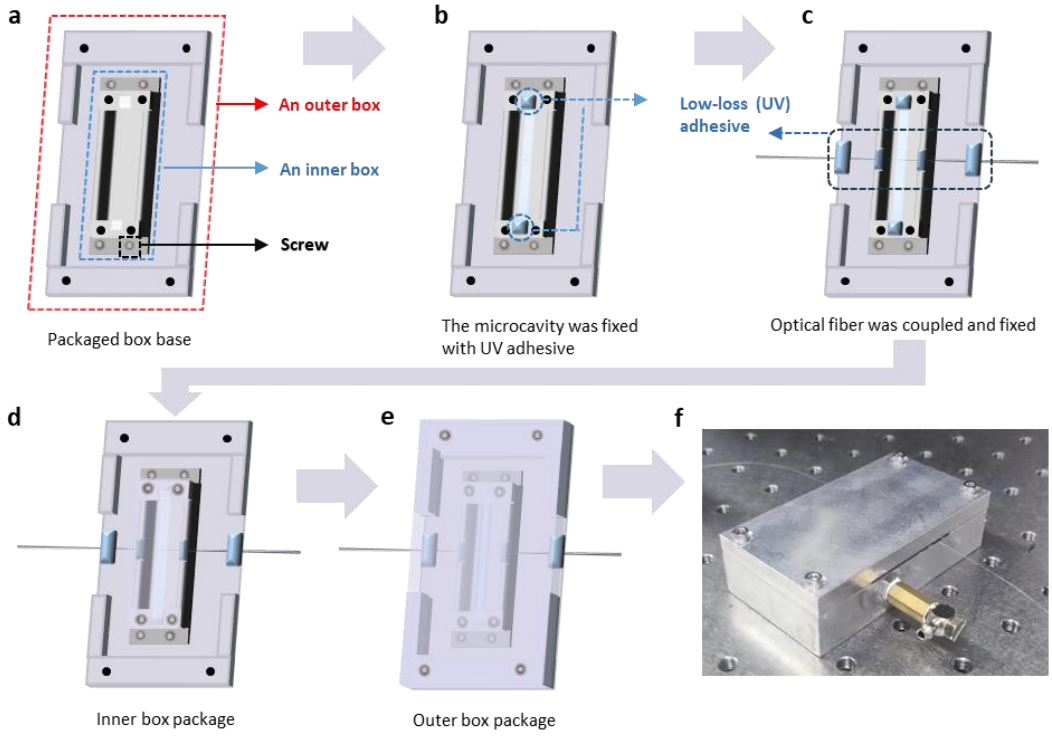

Fig. S4. Packaging process of the microrod cavities. a-e, Packaging process diagram. **f,** Packaged microrod cavity with nitrogen inlet devices.

Supplementary Note S3: Experimental measurement.

S3.1 Experimental measurements of *Q* factors.

Fig. S5 demonstrates our experimental setup for the transmission spectrum and quality factor measurements. A tunable ECDL (Santec TSL710) with a tuning range from 1480 nm to 1640 nm and a tuning speed of 1 nm/s works as the pump laser. A fiber polarization controller (FPC) is used to choose the proper polarization mode thus ensuring high coupling efficiency between the microfiber and the microrod cavity. The microrod cavity is fixed between two aluminum heat conducting elements, and the temperature is controlled by a thermoelectric cooler (TEC: Thorlabs TC200 & HT10K, resolution 10 mK). A 5 MHz MZI is used to calibrate the laser frequency during the ECDL sweep. The output signals are collected by photodetectors and then sent to the oscilloscope for analysis. A trigger signal is used to synchronize the ECDL and the oscilloscope.

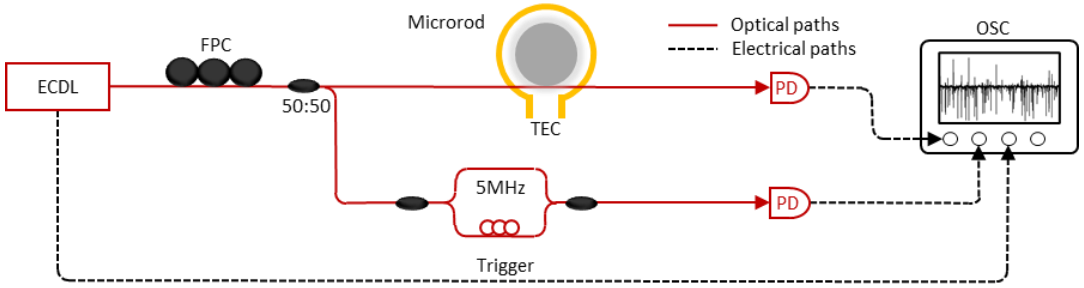

Fig. S5. Experimental setup for the transmission spectrum and quality factor measurements.

S3.2 Experimental measurements of *Q*-factor improvement.

Figure S6 plots the transmission traces as the Q_0-factor improves. During the heating and N_2 supply stage, the water vapor on the surface of the microcavity is gradually evaporated and brought out by the N_2, which significantly improves the Q factor of the microcavity to from 1.52×10^9 (**Fig S6a**), 4.45×10^9 (**Fig S6b**) to 8.13×10^9 (**Fig S6c**), corresponding to a longer photon lifetime. Then, stop heating and stop to supply N_2. During this process, the microcavity gradually cools down. Owing to the presence of hydroxyl groups on the cavity's surface, the re-absorption of water molecules from the atmosphere leads to a decrease of the intrinsic Q factor to 7×10^9 level (**Fig S6d**).

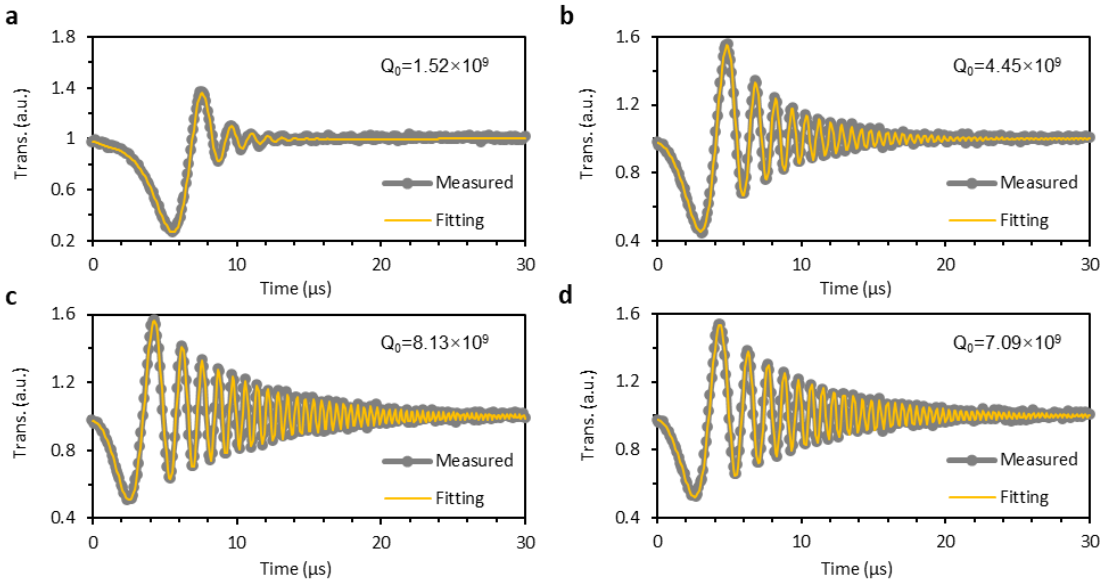

Fig. S6. Experimental measurement during Q_0 improvement process. Transmission traces before heating (**a**), heating & input N_2 (**b**), stop heating & keep N_2 environment (**c**) and cooling & stop N_2 (**d**).

S3.3 Experimental measurements of fully stabilized soliton microcomb based on microrod cavity.

S3.3.1 The locking process of fully stabilized soliton microcomb.

For a high repetition rate microcomb, the frequency of each comb line can be expressed as $f_n = f_p + nf_{rep}$, where f_n represents the frequency of the comb line corresponding to the mode number n, f_p represents the frequency of pump laser, and f_{rep} represents the repetition rate. Therefore, if the frequency of pump laser and n-th comb line can be stabilized at the same time, the entire optical frequency comb tooth can be locked. Based on this principle, a full stabilized soliton microcomb is realized by referencing the pump laser and the n-th comb line to the ultrahigh Q microrod. The experimental setup of fully stabilized soliton microcomb is shown in **Fig. 5a**. The system mainly includes three servo feedback loops: pump laser locking loop, reference laser locking loop and repetition rate locking loop.

The locking feedback steps of the pump and reference lasers are as follows: first, the pump laser (NKT-E15@1550 nm) and the reference laser (NKT-E15@1530 nm) were respectively passed through an acousto-optic modulator and then split into two paths using a 90:10 coupler; second, 10% of the modulated pump laser and reference laser are used for servo locking; third, the PDH technology is used to stabilize the output light of the AOM at the resonance peak of the microrod cavity, and the feedback signal is applied to the modulation frequency of the AOM to achieve laser frequency

stabilization.

The locking feedback steps of the repetition rate are as follows: first, the remaining 90% of the modulated reference laser and the output soliton microcomb are input into the photodetector together, and the reference laser will beat with the comb tooth with the closest frequency; second, the beat signal is mixed with a microwave reference to generate an error signal; third, the error signal is input into the servo, and the feedback signal acts on the output power of the auxiliary laser to achieve repetition rate stabilization.

S3.3.2 The characterization of pump laser and reference laser.

The characteristics of the pump laser and the reference laser are calibrated by a fully locked laser frequency comb (Menlo system FC 1500-ULNova-ORS, f_{rep}=250 MHz). The characterized setup is shown in **Fig. S7a**. The pump laser and the reference laser are respectively combined with the Menlo comb to generate a beat signal through a photodetector. Since the teeth of the Menlo comb have extremely low noise ($\leq 1\times10^{-16}$@1s, https://www.menlosystems.com/cn/products/optical-frequency-combs/fc1500-250-uln/), we believe that the noise of the beat signal comes entirely from the pump laser and the reference laser. **Fig. S7b** shows the optical spectrum of Menlo system laser comb, which covers 1450-1650 nm. The characterization of pump laser is shown in **Fig. 6**, and the characterization of reference laser is shown in **Fig. S8c-e.** The radiofrequency beatnotes (about 36.9 MHz) of the free running and stabilized reference laser acquired with an electrical spectral analyzer (Rohde & Schwarz FSW 43) are compared in **Fig. S7c&d**, demonstrating substantial narrowing of linewidth from 40 kHz to 400 Hz and significant improvement of stability from 5MHz to 0 MHz after locking. **Figure S7e** presents a comparison of single side band phase noise of the reference laser before and after locking. Within an offset frequency range of 1 Hz to 1 MHz, the noise suppression of reference laser is 48dB @ 1Hz and 25dB @ 10 kHz, respectively.

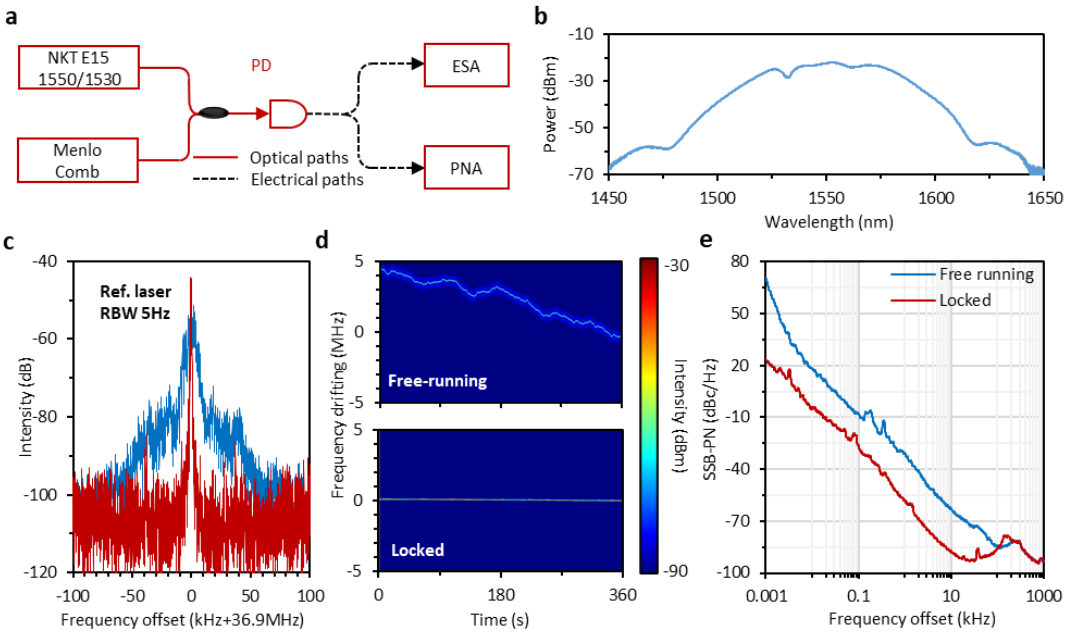

Fig. S7. The characterization of reference laser before and after locking. a, The characterized setup for pump laser and reference laser. **b,** The optical spectrum of Menlo system laser comb, covering 1450-1650 nm. **c-d,** The RF linewidth and long-term frequency stability of the reference laser before and after locking. **e,** The SSB-PN of reference laser before and after locking.

S3.3.3 The generation of soliton microcomb based on Si_3N_4 microring.

The remaining 90% of locked pump laser is used to excite a Si_3N_4 microring resonator with a loaded Q factor of 4×10^6 and a repetition rate of 100 GHz. Here we use the auxiliary laser method to generate soliton microcombs[5], which can provide feedback dimensions for locking the repetition rate while ensuring thermal stability in the cavity. However, unlike the tuning method of the traditional auxiliary laser, since the pump laser is locked to the reference cavity and cannot be tuned, we tune the temperature of the microring to move the resonance peak of the microring from low frequency to high frequency, ensuring that the pump laser is finally in the red detuning interval of the microring resonance peak. Then, we tune the frequency of the auxiliary laser so that it enters the microring from the blue detuning interval. At this time, the resonance frequency of microring redshift, and the pump laser enters the blue detuning interval, generating a chaotic comb. Then, the auxiliary laser blueshifts, the resonance peak blueshifts, causing the pump laser to enter the red detuning again, thus generating a soliton microcomb.

S3.3.4 The characterization of repetition rate.

Figure S8a shows the experimental setup for microcomb repetition rate

characterization. Since the 100 GHz repetition rate soliton microcomb cannot be directly characterized, a 21 GHz electro-optic modulator is used to generate sidebands. Thereby, we can obtain a beatnote signal with a frequency equal to the remainder of the repetition frequency divided by the modulation frequency (about 200 MHz) using a photodetector and characterized this signal using an electrical spectral analyzer (Rohde & Schwarz FSW 43) and a phase noise analyzer (Rohde & Schwarz FSPN 26). The spectrum after acousto-optic modulation is shown in the **Fig. S8b. Figure S8c** is the SSB-PN curve of the RF source used for modulation, which has much lower noise than the repetition frequency signal, so we believe that the noise of the beat-note signal modulated soliton microcomb comes entirely from the repetition rate noise.

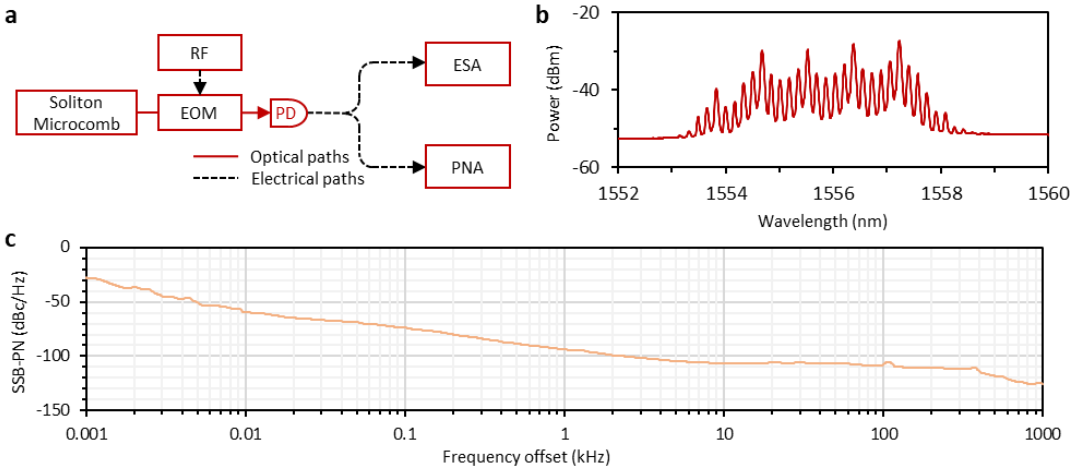

Fig. S8. Experimental measurement for microcomb repetition rate characterization. a, The experimental setup. EOM: electro-optic modulator, PD: photodetector, ESA: electrical spectral analyzer, PNA: phase noise analyzer. **b,** The spectrum after acousto-optic modulation. **c,** The SSB-PN of the RF source used for modulation.

References

1. Armani, D. K., Kippenberg, T. J., Spillane, S. M. & Vahala, K. J. Ultra-high-Q toroid microcavity on a chip. *Nature* **421**, 925–928 (2003).
2. Liu, T. *et al.* Optical microcombs in whispering gallery mode crystalline resonators with dispersive intermode interactions. *Photonics Res* **10**, 2866 (2022).
3. Gao, M. *et al.* Probing material absorption and optical nonlinearity of integrated photonic materials. *Nat Commun* **13**, 3323 (2022).
4. Weinstein, L. A. & Dutton, D. Open Resonators and Open Waveguides. *Am J Phys* **38**, 114–115 (1970).
5. Zhou, H. *et al.* Soliton bursts and deterministic dissipative Kerr soliton generation in auxiliary-assisted microcavities. *Light Sci Appl* **8**, 50 (2019).